Laser and Particle Beams (2004), *22*, 147–156. Printed in the USA.

DOI: 10.1017/S0263034604222091

Numerical studies on the ultrashort pulse *K*-α emission sources based on femtosecond laser–target interactions

J. LIMPOUCH,[1] O. KLIMO,[1] V. BÍNA,[1] AND S. KAWATA[2]

[1]Czech Technical University in Prague, Faculty of Nuclear Sciences and Physical Engineering, Praha, Czech Republic
[2]Utsunomiya University, Department of Electrical and Electronics Engineering, Yohtoh, Utsunomiya, Japan

(RECEIVED 12 June 2003; ACCEPTED 31 August 2003)

Abstract

K-α emission is an intense short-pulse line source well suited for X-ray diagnostic techniques with subpicosecond and micrometer resolution. Numerical simulations are performed here in a search for laser–target interaction regimes where both high efficiency of laser energy transformation to X-ray emission and ultrashort X-ray pulses are achieved. We use the one-dimensional PIC code for the description of the laser interaction with the plasma layer at the target surface. Fast electron transport into the target is treated by our newly developed Monte Carlo code with temporal resolution that is described here in detail. Our simulations reveal extremely short ~200 fs FWHM bright *K*-α X-ray pulses emitted from targets heated by 120-fs pulses of a table-top laser. Laser energy conversion efficiency to *K*-α line emission as high as 6×10^{-5} is noticed. Integration of the emitted energy over the focal spot is carried out to improve the simulation accord with published experimental data. Negligible impact of self-induced electric fields on *K*-α emission is found for conducting target materials at moderate laser intensities $\lesssim 10^{17}$ W/cm^2.

Keywords: Electron acceleration; *K*-α emission; PIC simulation; Time-resolved Monte Carlo code; Ultrashort-pulse laser–target interaction; Ultrashort X-ray pulse

1. INTRODUCTION

The rapid progress in the generation of intense femtosecond laser pulses has opened new opportunities for producing short pulse short wavelength radiation (Gibbon & Förster, 1996; Von der Linde *et al.*, 2001). Laser-driven radiation sources with picosecond pulse duration and photon energies ranging from 100 eV up to several megaelectron volts are now becoming available. It opens the way to experimental studies of the structure of matter with a unique combination of micrometer spatial and subpicosecond temporal resolution. Femtosecond X-ray pulses are required to resolve changes of the structure of a crystal lattice on its natural time scale 10^{-14}–10^{-13} s. Such X-ray pulses, synchronized with the incident laser pulse, are extremely important as diagnostic probes in the pump-probe experiments for observing the dynamic response of optically excited materials. This scheme has already been applied to observe the propagation of acoustic phonons in a crystal (Rose-Petruck *et al.*, 1999) and to detect ultrafast solid–liquid transition in semiconductors (Siders *et al.*, 1999; Von der Linde *et al.*, 2001) via X-ray diffraction with picosecond temporal resolution.

K-α emission is a particularly interesting X-ray line source, as the emitted energy may be comparable with the most intense resonance lines (often He-α line) or even higher (Nakano *et al.*, 2001), and the pulse length may be considerably shorter. While the intense resonance lines are emitted from femtosecond laser-produced plasmas for 10 ps or more (Andreev *et al.*, 2002), intense *K*-α pulses shorter than 250 fs have already been detected (Feurer *et al.*, 2001*a*). Moreover, the optimum laser intensities for efficient emission of short *K*-α pulses from low and middle *Z* elements are much below the relativistic threshold (Reich *et al.*, 2000), and thus, relatively small and cheap table-top femtosecond lasers with high repetition rates are suitable for laser-driven ultrafast X-ray sources.

K-α emission is eagerly studied, both experimentally and theoretically. The main laser pulse is often preceded by a prepulse. Sometimes, amplified spontaneous emission (ASE) forms a long nanosecond prepulse (Eder *et al.*, 2000; Zhidkov *et al.*, 2000). In other experiments, a short femtosecond

Address correspondence and reprint requests to: J. Limpouch, Faculty of Nuclear Sciences and Physical Engineering CTU, Břehová 7, 115 19 Praha 1, Czech Republic. E-mail: limpouch@siduri.fjfi.cvut.cz

laser prepulse is used in a controllable manner to improve the efficiency of laser energy transformation into K-α emission (Schlegel *et al.*, 1999; Uschmann *et al.*, 1999; Nakano *et al.*, 2001). An enhancement in K-α emission is found for the optimum pulse separation that is near to the time needed for the formation of the density scale length L_{opt} optimum for resonance absorption.

These experiments are typically modeled via a combination of hydrodynamic, one-dimensional (1D) PIC, and Monte Carlo codes. Hydrodynamic code is usually applied exclusively for determination of the plasma density profile at the main pulse arrival. The interaction of the main pulse with the target is treated via PIC code and the resulting fast electron distribution is the input for Monte Carlo calculations solving electron transport through the solid material and K-α emission. Monte Carlo codes without temporal resolution are commonly used, and then the emitted energy is derived only. Nevertheless, a Monte Carlo code with temporal resolution has been previously used (Feurer *et al.*, 2001*b*), and K-α pulses as short as 175 fs FWHM were found in simulations.

The duration, shape, and energy of K-α pulses emitted normally from the target front (laser) side are studied here in more detail for various laser and target parameters. The output of 1D3V PIC code, using a boosted frame to treat an oblique incidence of laser radiation, includes the time points when fast electrons cross the rear boundary of the PIC simulation box, as well as their velocity vectors. This is used as the input for our newly developed time-resolved three-dimensional (3D) Monte Carlo code "HEIKE" (Hot Electron Induced K-α Emission). The code follows fast electron trajectories through the target and records all events of K-shell ionization. Then the probability of K-α emission is taken into account and the photon transfer to the target boundary is tracked. Self-induced electric fields driving the return current may be included in our Monte Carlo code. An integration over the focal spot is also performed to resolve the discrepancy in K-α emission between experiments and simulations for small density scale lengths L (Schlegel *et al.*, 1999).

The simulation model is presented in Section 2. The newly developed time-resolved Monte Carlo code is described here in detail to demonstrate its unique features and versatility. The results of our simulations are presented and discussed in Section 3. In the last section the conclusions are summarized and our plans for future research are briefly discussed.

2. SIMULATION TECHNIQUE

Interactions of short laser pulses with thick solid targets are studied here. The simulation is split into two regions: the corona, treated by 1D3V PIC code, and the cold solid target where the transport of fast electrons is modeled by our Monte Carlo code and where K-α photons originate. This split is presented schematically in Figure 1.

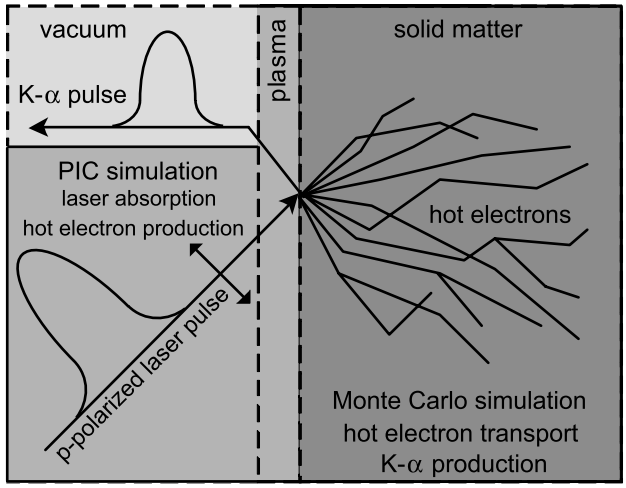

Fig. 1. The scheme of our simulation split into two regions. Absorption of p-polarized femtosecond laser pulse obliquely incident on the target and hot electron production is treated by PIC simulation; hot electron transport and K-α production and transport are treated by Monte Carlo code. Zero width transitional region is assumed.

Fast electrons escaping from the corona region into the target are substituted by a flux of Maxwellian electrons with initial electron temperature T_{e0}. Fast electrons crossing the rear boundary of the PIC simulation box are the input for the Monte Carlo simulations. Fast electron reflection from the target rear side is negligible in thick targets. Moreover, we do not take into account a possibility that a fast electron could reenter the interaction region, though a portion of fast electrons are scattered backwards in Monte Carlo simulations. First, most of the backscattered electrons could reenter the corona only after the termination of a femtosecond laser pulse. Second, most of the backscattered electrons are relatively low-energy electrons and thus their substitution by electrons from the thermal distribution does not lead to a substantial error. Consequently, Monte Carlo code is used here as a postprocessor to the PIC simulations.

We assume here a steplike boundary between hot corona region and cold solid matter. A jump in electrostatic potential on the boundary may be added. This is certainly an approximation because a transitional region of dense plasma exists and it was previously modeled by hydrodynamic simulations (Davis *et al.*, 1995). However, the thickness of the transitional region will be typically considerably less than 1 μm for the experimental parameters studied here whereas the typical depth of the K-α emission region is 10 μm. Moreover, a typical ion charge in the transition region will be higher than 4+ and K-α emission of these ions can be spectrally resolved from the cold solid-matter emission. The cross sections for the fast electron transport are less known in heated dense plasmas than in the solid matter. Also, it would be very time consuming to use both temporally and spatially varying target parameters in our time-resolved Monte Carlo simulations, though it is possible in principle.

https://doi.org/10.1017/S0263034604222091 Published online by Cambridge University Press

Thus, we take into account here only *K*-α emission from cold solid matter that can be, in principle, spectrally resolved from corona emission. If the emission from the heated plasma is not spectrally separated, it may also influence the measured temporal profile of X-ray pulse. The typical time scale of the corona cooling will be up to 10 ps and thus a short peak of fast-electron-induced *K*-α emission will appear on a much longer background emission. This may lead to measured emission pulse durations much longer than expected (Nakano *et al.*, 2001). If thin surface layer (typically 1–2 μm) of low-*Z* material is used, the experiment may be substantially clearer and our model will be more realistic.

A detailed description of our PIC and Monte Carlo codes follows in specialized subsections.

2.1. PIC code

Our PIC code evolved from LPIC++ code (Lichters *et al.*, 1997), which was developed at Max–Planck–Institute für Quantenoptik in Garching, Germany. The code is based on a one-dimensional, electromagnetic, relativistic algorithm, where all three velocity components are included, and thus interactions of circularly polarized laser waves with plasmas can be modeled. The code enables us to study the oblique incidence of laser radiation by using a boosted frame via relativistic Lorentz transformation.

The code was originally intended for studies of laser interaction with thin foil targets. Thus, electron specular reflection on both boundaries was assumed. Here, the electrons crossing the corona–target boundary are substituted by a return current of thermal electrons. When an electron hits the rear simulation box, it is substituted by an electron with a random velocity with the probability proportional to $-v_z \exp(-\varepsilon/T_{eb})$, where only negative normal components v_z of velocity are allowed, ε is electron relativistic kinetic energy, and electron temperature T_{eb} in energetic units behind the rear boundary is set here equal to the initial electron temperature T_{e0}.

The original code was collisionless. We have included elastic electron–electron, electron–ion, and ion–ion collisions (Limpouch *et al.*, 2002) using the Takizuka–Abbe method. Our fully relativistic treatment of elastic collisions may be used in the boosted frame. Tests carried out for laser incidence angles up to 30° proved that no influence of elastic collisions on fast electron spectra may be detected within the simulation accuracy for the conditions assumed here. Consequently, all presented simulations are collisionless.

The original code was parallelized by using the PVM (Parallel Virtual Machine) library. PVM is now considered outmoded and often it is not implemented at new parallel machines, so the code was modified to use modern Message Passing Interface (MPI) library. Excellent parallel performance of our code enables the use of a large number ($>10^6$) of macroparticles to suppress noise.

2.2. Monte Carlo code

Monte Carlo simulations are often applied for detailed studies of fast electron transport in solid materials and of the induced events (e.g., inner-shell ionization, bremsstrahlung emission). Many Monte Carlo codes are specialized on the transport of high-energy electrons with energies above 100 keV. Some codes are universal, both for high- and low-energy electrons. Widely spread Monte Carlo code PENELOPE (Salvat *et al.*, 2001) is perhaps the best known example of this category. However, the model of *K*-shell ionization is not very sophisticated in PENELOPE and the code also does not allow for temporal resolution. To our knowledge, no available code can meet our requirements in both of these key issues, and thus we have developed our own code "HEIKE." Increasing computer performance allowed us to use the so called "single scattering" model, with both elastic and inelastic collisions simulated directly.

In our code, elastic collisions are described by screened Rutherford cross section or, at lower electron energies, by the semiempirical formula for Mott cross section derived by Browning (Browning *et al.*, 1995). This technique is not computationally fast, but for the case of our study, when not so many high-energy electrons are present, the performance of the code was sufficient. Inelastic collisions are described by cross sections similar to those used in PENELOPE code (Salvat *et al.*, 2001). These cross sections are based on the generalized oscillator strength model and the incident electron is assumed to interact with a single electronic shell of the target atom. The cross sections are doubly differential, both in the scattering angle and in the energy loss, and they are also suitable for a simulation of fast secondary electron generation, which is also included in our code. Bremsstrahlung emission does not play an important role for our conditions—rather low-*Z* target materials and rather low fast electron energies. Thus, the impact of bremsstrahlung on fast electron transport was approximated by continuous slowing down with the stopping power taken from the National Institute of Standards and Technology (NIST) database ESTAR (Berger *et al.*, 2000).

The cross sections for inelastic collisions already include *K*-shell ionization as one of the interactions; however, its probability is systematically underestimated in this model. Consequently, another more accurate semiempirical cross section (Casnati *et al.*, 1982) for *K*-shell ionization is used. *K*-shell ionization using this cross section was simply added into already correct fast electron transport code. After each trajectory step, the code samples the probability that *K*-shell ionization occurred, but it leaves the electron parameters unaltered. The position and time of *K*-shell ionization is sampled uniformly along the trajectory step. The same method was also used by Acosta *et al.* (1998).

When *K*-shell ionization occurs, an ionized atom relaxes very quickly on the femtosecond time scale to a lower energetic state. The probability that *K*-α photon is emitted during this relaxation, the fluorescent yield, is assumed to

https://doi.org/10.1017/S0263034604222091 Published online by Cambridge University Press

be 0.042 for Al according to Davis *et al.* (1995). *K-α* transport in the target is then simply approximated by Beer's law of exponential attenuation. The mass attenuation coefficient is taken from the NIST database (Hubbel & Seltzer, 2001).

As we also need information about the duration and temporal profile of the *K-α* pulse, the time resolution is included in the code. The time is simply recalculated after each trajectory step from the fast electron velocity and the step length. Other interesting options of the code include a possibility to model multilayer targets with up to five layers from different materials, and a partial or total electron reflection at the border of each layer. The database presently comprises the following materials: Al, Cu, Si, Ti, and polyethylene.

The electron trajectories in Monte Carlo simulations are mutually independent; hence, the code may be parallelized simply and its performance may be significantly enhanced. Typically, the trajectories of $\sim 10^7$ fast electrons are tracked in our Monte Carlo simulations. The correctness of the code was tested for monoenergetic electron beams via simulations of electron backscattering yields and via simulations of *K-α* emission from the target front side. A good agreement with both experimental and computed data was found. The comparison of the resulting *K-α* emission yields from aluminum targets with experimental results of Dick *et al.* (1973) and with the Monte Carlo electron transport code EGS4 (Namito & Hirayama, 1999) is demonstrated in Figure 2. One can notice that the energy of *K-α* emission is maximum for the electrons with an energy of approximately 60 keV. Unfortunately, the data for comparison are available only for 40 keV and 100 keV in the region of maximum *K-α* yield, and thus one cannot exclude the possibility of a certain inaccuracy in the code.

Self-generated electromagnetic fields may influence fast electron transfer to solid targets (Davies *et al.*, 1997). Two possible sources of these fields are included in our Monte Carlo code. First, the electric field in the transitional region between the corona and the dense solid matter may be approximated by a potential jump at the entrance of the Monte Carlo simulation region. The potential jump does not allow low energy electrons to enter the solid matter and it decreases the longitudinal velocity of high-energy electrons. Second, an electric field can be applied in the Monte Carlo region, and electron trajectories are then calculated in the assumed electric field. Our time-resolved Monte Carlo code makes calculation of spatial–temporal behavior of fast electron current possible. If the electric conductivity of the target material is known, one can compute the electric field that is needed to drive the return current. In principle, an iteration procedure may be applied to evaluate the induced electric field self-consistently. However, we have included this option with the goal of qualitative assessment of the field impact.

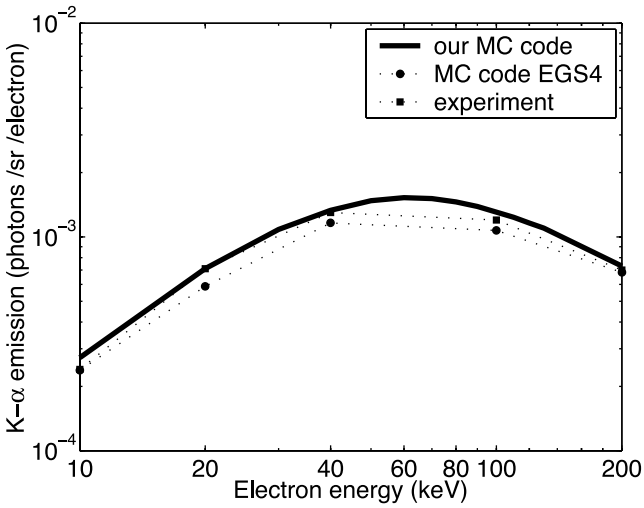

Fig. 2. Number of *K-α* photons emitted normally from Al target front side per steradian per one electron in a monoenergetic electron beam incident normally on the target.

3. RESULTS AND DISCUSSION

The simulations presented here take the basic laser parameters from Schlegel *et al.* (1999). As the prepulse focal spot is significantly broader than that of the main laser pulse in experiment, one can assume that the main pulse interacts with a planar expanding plasma. The experimental pulse separation was varied between 0 and 20 ps. Both, analytical model and hydrodynamic simulations (Schlegel *et al.*, 1999) show that exponential profiles with density scale lengths $L \lesssim \lambda$ approximate well the plasma density profile at the main pulse rise. P-polarized Ti:Sapphire ($\lambda = 800$ nm) 120-fs FWHM main laser pulse of maximum intensity $I_m = 4 \times 10^{16}$ W/cm^2 was incident at the angle $\theta = 45°$ to the target normal. Thick solid SiO_2 targets were used in the experiment, and measured Si *K-α* emission energies were absolutely calibrated. Comparison with numerical simulation was also presented.

Basically, we assume here solid aluminum targets, and *K-α* emission from solid copper is calculated for comparison. Aluminum is the next element to Si, so the dependence of *K-α* emission on fast electron energy is very similar. Aluminum is treated more simply than SiO_2 compound in Monte Carlo calculations. Moreover, aluminum is a good conductor and, consequently, the impact of self-induced electromagnetic fields on the fast electron transport is minimized. *K-α* emission yields from Al targets were studied for similar, but slightly different laser conditions by Nakano *et al.* (2001), where the measured emitted energies were only relatively calibrated.

3.1. Fast electron spectra from PIC simulations

Our 1D3V PIC simulations describe the interaction of the main laser pulse with an expanding plasma created by the prepulse. The initial plasma density profile in PIC simulations is assumed exponential up to a certain maximum

https://doi.org/10.1017/S0263034604222091 Published online by Cambridge University Press

electron density n_{max} and then a density plateau of length L_p is added up to the rear boundary of the simulation box. The plateau length is set at $L_p = \lambda$ for the longest scale length $L = \lambda$ whereas slightly larger lengths L_p are chosen for steeper density profiles in order to keep the total electron number inside the PIC simulation box constant. Usually, the maximum electron density is set $n_{max} = 10\ n_c$, where n_c is the critical density. In a few simulations, higher electron density $n_{max} = 30\ n_c$ has been assumed; however, the impact of higher maximum density on the fast electron spectrum was negligible. Mean ion charge Z of aluminum plasma was frequently set to $Z = 10$. This ion charge is highly overestimated at the rise of the main pulse, and a few runs have been conducted with $Z = 7$ and $Z = 3$. The decrease in mean charge Z generally leads to a slight reduction in the energy of fast electrons. While the differences in the *K-α* yield between the cases $Z = 7$ and $Z = 10$ were negligible, ~20% reduction in the *K-α* yield was observed when the mean ion charge was decreased to $Z = 3$ for very short density scale lengths L. The impact of the transient ionization processes may be correctly modeled only via PIC codes that take into account collisional ionization (Zhidkov *et al.*, 2000).

The time of the event when an electron crosses the rear PIC simulation box boundary is recorded together with the electron velocity vector for the postprocessing by our Monte Carlo code. Only electrons capable of inducing *K*-shell ionization (electrons with energy $\varepsilon > 1.5$ keV for Al) are recorded. The spectra of these electrons are plotted in Figure 3. Figure 3a shows the dependence of the fast electron spectrum on the plasma parameters and on laser intensity for very small density scale length $L = 0.001\lambda$. The decrease in the initial electron temperature T_{e0} from 600 eV to 100 eV lowers the number of electrons with energies less than 5 keV considerably, as practically no thermal electrons with energy $\varepsilon > 1.5$ keV exist for the lower electron temperature. A slight decrease in the maximum electron energy from 95 keV to 85 keV is also observed. The main part of the fast electron spectrum between 5 keV and 60 keV is practically unchanged; a small enhancement of electron number between 15 and 20 keV is compensated by a decrease above 50 keV. As the probability that an electron with an energy below 5 keV induces *K-α* photon emission is extremely low and as the number of electrons above 60 keV is very small, *K-α* emission is virtually independent of the initial temperature T_{e0} in PIC simulations. Smaller plasma mean ion charge Z in PIC simulations leads to a certain decrease in number and energy of fast electrons. However, even at the lowest limit, $Z = 3$, this decrease is much less than in the case when three times smaller laser intensity is assumed.

Fast electron spectra are plotted for various density scale lengths L in Figure 3b. Maximum fast electron energies, as well as maximum total energy in fast electrons, are observed for the density scale length $L = 0.2\lambda$ near to the classical optimum for resonance absorption $(k_0 L_{opt})^{2/3} \sin^2\theta \simeq 0.6$. However, an excessive number of electrons with energies in the range 20–60 keV is observed for the sharp density profiles $L \lesssim 0.05\lambda$. The observed fast drop in the number of these electrons for larger L might possibly support a hypothesis about their production by the vacuum heating mechanism (Brunel, 1987). As the efficiency of the energy transformation to *K-α* emission escaping from the target front side is particularly high in aluminum for the above electron energies (see Fig. 2), *K-α* yield may be even higher for very sharp density profiles than for the optimum density scale length L_{opt}.

Fast and thermal electrons also differ in their angular characteristics. Whereas thermal electron velocities are isotropic, fast electrons are well collimated nearly normally to the target surface. The angular spectrum of electrons leaving PIC simulation box with energies $\varepsilon > 1.5$ keV is shown

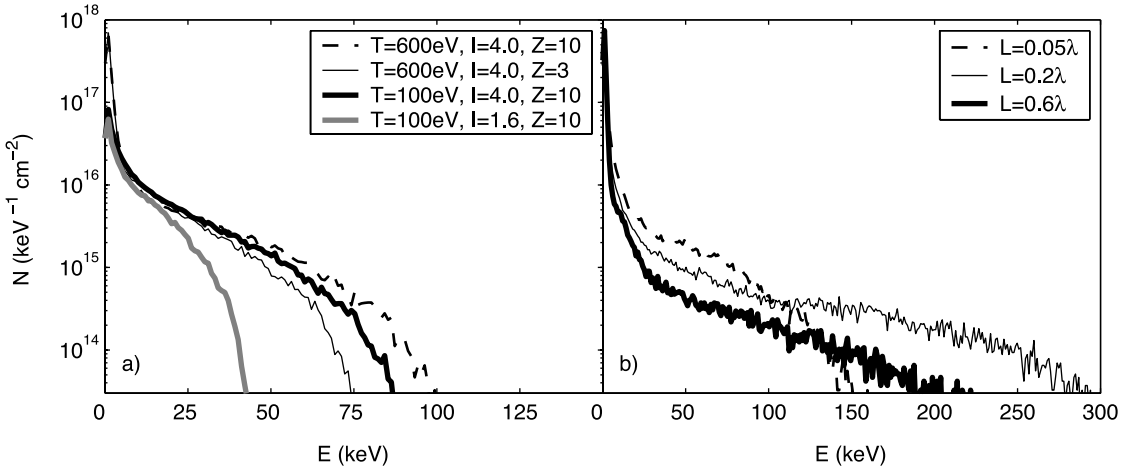

Fig. 3. Energy spectra of hot electrons crossing the rear boundary of the PIC simulation box into the target. The spectra are plotted for the density scale length L = 0.001λ (a) for the indicated values of the initial electron temperature *T*, of mean ion charge *Z*, and of the maximum intensity *I* (in units of 10^{16} W/cm^2) of the 120-fs FWHM p-polarized laser pulse incident at angle 45°. The dependence of hot electron spectrum on the density scale length *L* is demonstrated (b) for the parameters $T = 600$ eV, $Z = 10$, and $I = 4 \times 10^{16}$ W/cm^2.

https://doi.org/10.1017/S0263034604222091 Published online by Cambridge University Press

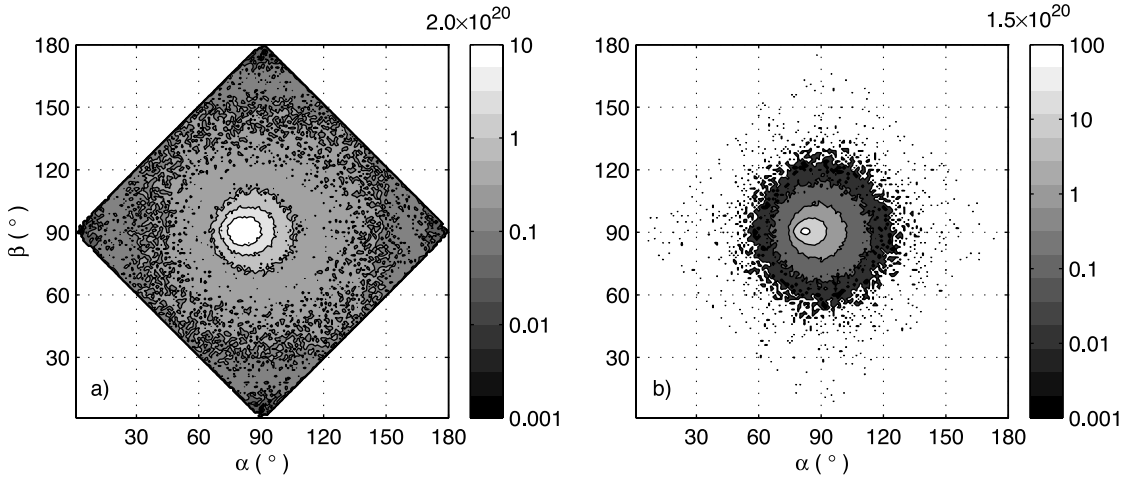

Fig. 4. Energy in hot electrons crossing the PIC simulation box rear boundary in the specified direction in units of keV/sr/cm^2. Angles α and β are angles with axes in the plane parallel with the target surface; the incident laser beam propagates in the direction $\alpha = 45°$ and $\beta = 90°$. The direction $\alpha = \beta = 90°$ is the normal into the target. The assumed PIC simulation parameters are the density scale length $L = 0.001\lambda$, mean ion charge $Z = 10$, and the maximum laser intensity of I $= 4 \times 10^{16}$ W/cm^2. The initial electron temperature is $T =$ 600 eV (a) and $T = 100$ eV (b).

in Figure 4 for two different initial electron temperatures T_{e0}. Energetic thermal electrons are present for $T_{e0} = 600$ eV and they form the broad less intense angular region in Figure 4a. Such thermal electrons are practically absent for $T_{e0} = 100$ eV (Fig. 4b), and the fast electron flux is concentrated to a cone of angle $\sim 15°$ with its center shifted for approximately 10° from the target normal to the direction of the incident laser beam propagation.

3.2. Temporal and energetic characteristics of *K*-α emission

Our Monte Carlo code follows all trajectories of the fast electrons inside a solid target from the instant when they leave the PIC simulation box. The code records the times and places of *K*-shell ionization events. The resulting highly unstable ions relax either via Auger electron or photon emission. The fluorescent yield for *K*-α photon emission is taken into account. On the other hand, the interval between ionization and photon emission is neglected here, because of very small relaxation time $\tau_r \lesssim 10$ fs. The times and depths of the *K*-α photon emission events are plotted in Figure 5 for the sharp plasma density profile and for the profile with the density scale length L_{opt} (optimum for resonance absorption). Very energetic electrons, typical for the density scale length L_{opt}, penetrate deep into the target and induce *K*-α photon emission there. However, these photons have a small chance to penetrate to the target front

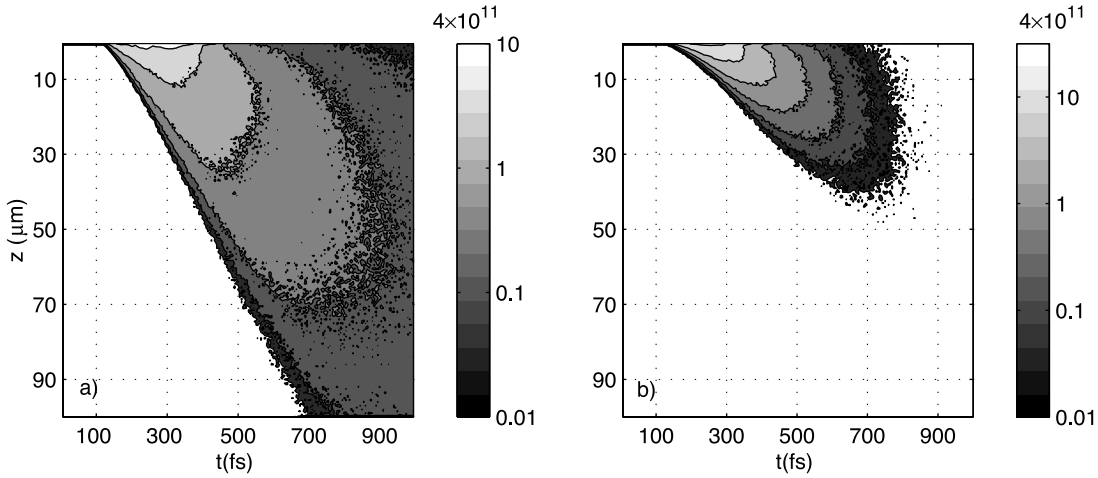

Fig. 5. Number of *K*-α photons/cm^2/fs/μm originating at time t in the specified target depth z. The simulation parameters are $I = 4 \times 10^{16}$ W/cm^2, $Z = 10$, $T = 600$ eV. The laser pulse maximum at the target is at $t \simeq 200$ fs. Plasma density scale length $L = 0.2\lambda$ (a) and $L = 0.001\lambda$ (b).

https://doi.org/10.1017/S0263034604222091 Published online by Cambridge University Press

side as the absorption length of *K-α* photons is ≃20 μm for aluminum. This figure illustrates the spatial–temporal profile of *K-α* emission that could, in principle, be recorded experimentally in the side view by using a target of a small width (e.g., wire or foil embedded in low-*Z* material normally to the laser target surface).

When the absorption and time delay during photon propagation to the target front side is taken into account, the temporal profile of the emitted pulse is obtained. Temporal profiles of the pulses emitted normally from the target laser side are plotted in Figure 6 for various density scale lengths *L*. The emission from aluminum is plotted in Figure 6a, and Figure 6b demonstrates *K-α* emission from copper. We should note that the same incident fast electron spectra are used both for aluminum and copper, strictly speaking Figure 6b represents copper emission from a target with a thin submicron aluminum layer on its surface. However, the result for pure copper targets should have only very minor differences for the same density scale length, as electron temperature, mean ion charge, and ion mass number have only a very small impact on the fast electron spectrum. It is worth noting that a different pulse separation may be needed for a copper target in order to produce the same density scale length *L* as in aluminum.

The calculated pulses of *K-α* emission are very short. The typical pulse duration is ≃180 fs FWHM for aluminum and ≃250 fs FWHM for copper. The pulse duration is practically independent of the density scale length *L*, and thus application of a prepulse does not lead to a prolongation of *K-α* emission. This is different from the case of resonance line emission, where the pulse prolongation was observed in simulations (Andreev *et al.*, 2002). The emitted pulses are asymmetric with a longer trailing edge. It is specially apparent for the density scale length L_{opt} where the trailing edge up to 500 fs is observed. *K-α* emission starts later for long density profiles due to the delay caused by the electron transit through the plasma corona. The temporal shifts between pulses emitted for different density scale lengths are smaller than their width. Even smaller pulse shifts are observed when laser intensity is varied for the same density scale length *L*. This is important because it means that laser intensity variations over the focal spot do not automatically lead to a significant prolongation of the *K-α* pulse. Of course, it might not be true for other two-dimensional effects. For instance, lateral fast electron transport in the corona may delay the time significantly when a certain portion of fast electrons enters the solid target. Two-dimensional PIC simulations have to be applied to assess such effects and we plan to address this question in the near future. The emitted intensity decreases with the density scale length *L* for aluminum, whereas for copper it maximizes at the optimum density scale length L_{opt}. It is the consequence of the assumed laser intensity that is too high for aluminum whereas it is near to the optimum for copper.

From the application point of view, it is very important to achieve the highest possible efficiency of the laser energy transformation into *K-α* emission. Often, laser intensity may be varied by positioning the target out of the best laser focus (Eder *et al.*, 2000). The number of *K-α* photons emitted normally from the target per unit solid angle is normalized on the laser energy in joules and it is plotted versus laser intensity in Figure 7a. Fast electron energies are rather low for sharp density profiles ($L \lesssim 0.05$), and relatively high intensity is required to accelerate electrons to energies around 50 keV that are optimum for *K-α* emission. So the energy transformation efficiency is maximum at laser intensity $I_m = 4 \times 10^{16}$ W/cm^2 or higher. For the density scale length $L = 0.6\lambda$, the transformation efficiency is maximum at laser intensity $I_m \simeq 1.6 \times 10^{16}$ W/cm^2, as fast electron energies are here only slightly higher than for $L = 0.001\lambda$. The absolute maximum of the energy transformation efficiency is achieved for the optimum density scale length L_{opt} at relatively low laser intensities $I_m \simeq 4 \times 10^{15}$ W/cm^2. Fast electrons are too energetic for higher laser

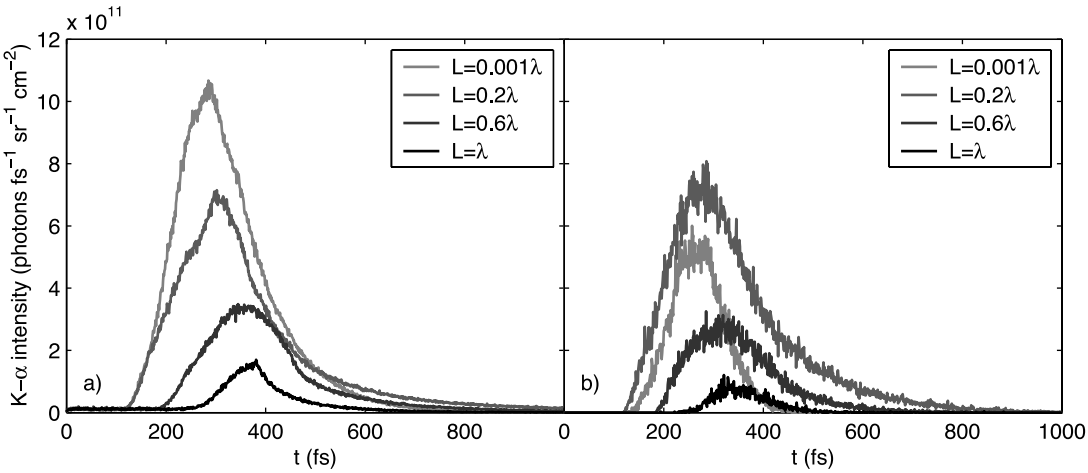

Fig. 6. The *K-α* pulses emitted normally from the target front surface for various plasma density scale lengths *L*. The laser and target parameters in PIC simulations are the same as in the previous figure. The materials are aluminum (a) and copper (b).

https://doi.org/10.1017/S0263034604222091 Published online by Cambridge University Press

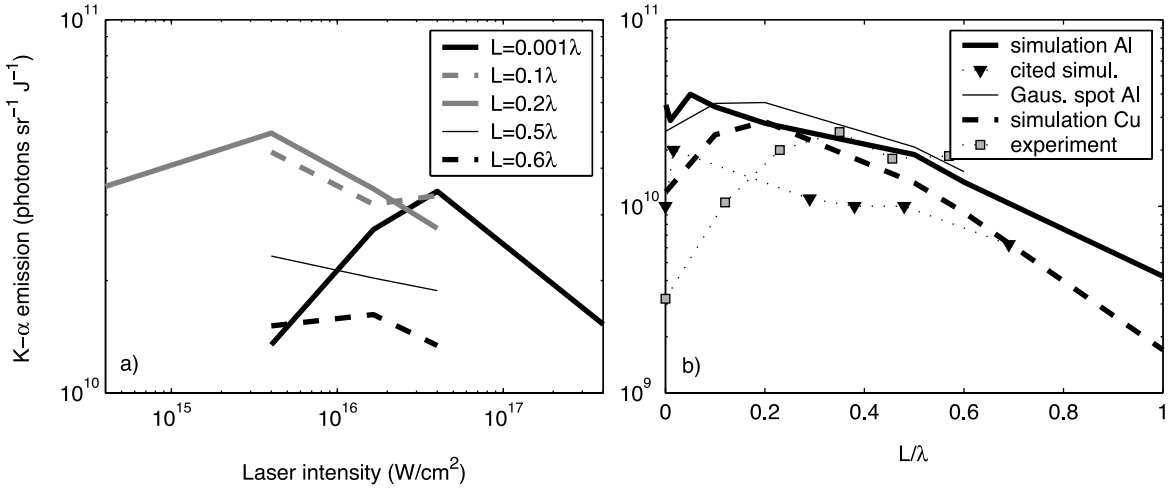

Fig. 7. a: The *K*-α emission normalized on the laser energy versus laser intensity for various density scale lengths L. b: The dependence of *K*-α emission on the density scale lengths L for the maximum laser intensity $I = 4 \times 10^{16}$ W/cm^2. The results of our simulations for Al and Cu and constant laser intensity are compared with our results for Gaussian laser beam (Al target) and with the experimental and simulation data for SiO_2 targets taken from Schlegel *et al.* (1999).

intensities, and *K*-α photons are produced too deep inside the target, so the probability of their escape from the target is very low.

The number of *K*-α photons emitted normally from the target is drawn in Figure 7b versus the density scale length L and it is compared with experimental and simulation data, taken from Schlegel *et al.* (1999). The separation of the prepulse and main pulse was varied in the experiment and the respective plasma density scale lengths were taken from one-dimensional hydrodynamic simulations. The experimental curve grows significantly with the density scale length L for sharp density profiles. It reaches its maximum at a density scale length L approximately 50% larger than the density scale L_{opt} optimum for resonance absorption and it sinks rather slowly. On the other hand, the calculated emission is maximum at rather low $L = 0.02\lambda$, and then it continually decreases. Our simulations, conducted for aluminum targets, result in qualitatively similar results with maximum emission at $L = 0.05\lambda$. The observed small emission decrease between $L = 0.001\lambda$ and $L = 0.01\lambda$ may be attributed to a decrease in vacuum heating, but this is purely an academic question because special precautions eliminating low-energy prepulse are required to achieve $L \lesssim 0.01\lambda$ in experiment. On the other hand, the simulations predict maximum *K*-α emission from copper for the density scale length L_{opt} optimal for resonance absorption. In copper, due its higher Z, the number of *K*-α photons emitted per one electron is maximum at relatively high electron energy $\varepsilon \simeq$ 200 keV. For the assumed laser intensity, such electrons are produced mainly at the density scale length L_{opt}. Due to higher energy of the *K*-α photon, the energy transformation efficiency η is higher in copper than in aluminum. For an estimate, we set the effective *K*-α emission angle equal to π. Then the maximum efficiency of laser energy transformation into *K*-α emission is $\eta \simeq 2 \times 10^{-5}$ for Al, and $\eta \simeq 6 \times 10^{-5}$ for Cu.

The above results have been obtained for constant laser intensities. However, laser intensity is inhomogeneous in any focal spot. If the laser intensity in the focus center is higher than optimum for *K*-α emission, then an area with optimum laser intensities exists at the edge of the focal spot. For the supposed laser parameters and *K*-α emission from an aluminum target, the effective surface of the focal spot is maximum for the density scale length L_{opt}. To estimate the impact of the laser intensity profile over the focal spot, a Gaussian laser beam is assumed, and the fast electron spectrum is supposed to depend purely on the local laser intensity as in Eder *et al.* (2000). The curve obtained by the integration of *K*-α emission yield over the focal spot is also included in Figure 7b. The resulting emission yield increases with the density scale length L for sharp density profiles, and a profound maximum is observed at L_{opt}. The curve is qualitatively more similar to the measurements; however, the enhancement of *K*-α yield by the laser prepulse in simulations is less than in experiment and the decrease of the emission yield at large pulse separations (large L) is faster in simulations.

The above results do not take into account electromagnetic fields induced by the energy transport into the target. A significant impact of these fields has already been confirmed for high laser intensities $I_m \gtrsim 10^{18}$ W/cm^2 (Davies *et al.*, 1997). We want to find out whether these fields are important for much smaller laser intensities assumed here.

First, we would like to estimate the electrostatic potential U_b slowing down electrons in the transitional layer between the corona and cold target material. Simple estimates show that the current density j_T of inward moving thermal electrons associated with heat flux may be up to 30× greater

https://doi.org/10.1017/S0263034604222091 Published online by Cambridge University Press

than the maximum current density of hot electrons $j_h \simeq 3 \times 10^{12}$ A/cm^2 in our simulations. Consequently, the return current has to compensate the flux of thermal electrons. Nevertheless, electric potential $U_b = T_e \ln(j_T/j_h)$ will decrease the current j_T of Maxwellian thermal electrons with temperature T_e to the level of the hot electron current j_h. The electric potential of about 2.5 kV was observed in the transition layer in Fokker–Planck simulations (Limpouch *et al.*, 1994) of the interaction of normally incident laser beam of intensity 10^{17} W/cm^2 with solid density aluminum plasma. As an upper estimate, a potential jump of 5 kV was introduced at the front boundary of the Monte Carlo simulation region. The decrease of *K-α* yield was rather small, less than 10% in the worst case of sharp density profile.

Second, one would like to estimate the impact of the electric field inside the solid target. Electric field E_s is required to drive the return current compensating the hot electron current j_h. Electric conductivity of solid aluminum has a minimum $\sigma \simeq 2 \times 10^6$ Ω^{-1}m^{-1} at a temperature of about 50 eV. Thus, $E_s = j_h/\sigma \simeq 1.5$ kV/μm is the electric field upper estimate. The impact of such an electric field on *K-α* emission is negligible. Thus, self-generated fields may be disregarded in the assumed conditions, at least for good conductors.

4. CONCLUSIONS

We have conducted a systematic numerical study of the dependence of *K-α* emission characteristics on laser and target parameters. The simulations have been performed via 1D3V PIC code supplemented by our newly developed three-dimensional Monte Carlo code "HEIKE" with temporal resolution. It uses hot electron data from the PIC simulations as an input. The transport of hot electrons is treated via an accurate, but computationally demanding single scattering model. *K*-shell ionization is modeled in detail via a specialized sophisticated cross section. Self-induced electromagnetic fields may be taken into account in a crude approximation. Temporally and spatially resolved *K-α* photon generation data are obtained and radiation transport to the target surface is included.

Hot electron spectrum was found to be nearly independent of the maximum electron density and of the initial electron temperature used in PIC simulations. Both maximum kinetic energy of hot electrons and the total laser energy transferred into hot electrons are increased at plasma density scale length L_{opt} optimum for resonance absorption, that is, when laser prepulse is applied with a proper pulse separation. Hot electrons are collimated to a cone nearly normal to the target surface.

Very short *K-α* emission pulses were observed in simulations. Laser pulse duration of 120 fs FWHM was assumed, and *K-α* pulses were less than twice longer (~180 fs for Al and ~250 fs for Cu). Emission pulse duration does not vary significantly with the density scale length *L*.

Hot electron energy optimum for *K-α* emission exists for each target material and it grows with material atomic number. If hot electron energies are greater, many photons are generated too deep to be capable of escaping from the target. For any density scale length *L* optimum laser intensity exists where the laser energy transformation to *K-α* emission is maximum. The optimum laser intensity is minimal for $L = L_{opt}$, and this point is the absolute maximum of the energy transformation efficiency.

We have used the integration over the focal spot in an attempt to reproduce experimental dependence of the *K-α* emission energy on the density scale length *L*. For low laser intensities, the energy transformation efficiency is maximum at the density scale length L_{opt}. For this scale length the relative contribution of lower intensities at the focal spot edge is maximum. Consequently, the effective focal spot area for *K-α* emission is enlarged for the density scale length L_{opt}.

We have found that at least for targets made of good conductors, the impact of the self-induced electromagnetic fields on *K-α* emission is negligible at moderate laser intensities below 10^{17} W/cm^2.

In the future we plan to use more elaborate PIC codes together with our Monte Carlo codes. First, the impact of the transient ionization on hot electron spectra may be studied using PIC code including ionization processes. Second, a two-dimensional PIC code may address the impact of the focal intensity profile on the *K-α* emission energy, emission area, and pulse duration.

ACKNOWLEDGMENTS

The authors thank Professor Jürgen Meyer-ter-Vehn for his kind gift of the original LPIC++ code. Fruitful discussions with Prof. L. Kocbach and Prof. L. Drŝka are acknowledged. This research was supported by the Grant Agency of the Czech Republic, contract No. 202/01/0755 and by INTAS, Brussels, Belgium, grant INTAS-01-0233. Parallel computation facilities were provided by the Bergen Computational Physics Laboratory within the EC activity "Access to Research Infrastructures" (contract HPRI-CT-1999-00094) and by the METACenter project of the Czech Universities.

REFERENCES

Acosta, E., Llovet, X., Coleoni, E., Riveros, J.A. & Salvat, F. (1998). Monte Carlo simulation of x-ray emission by kilovolt electron bombardment. *J. Appl. Phys.* **83**, 6038–6049.

Andreev, A.A., Limpouch, J., Iskakov, A.B. & Nakano, H. (2002). Enhancement of x-ray line emission from plasmas produced by short high-intensity laser double pulses. *Phys. Rev. E* **65**, 026403.

Berger, M.J., Coursey, J.S. & Zucker, M.A. (2000). Stopping power and range tables for electrons, protons, and helium ions: ESTAR. National Institute of Standards and Technology, http://physics.nist.gov/PhysRefData/Star/Text/contents.html.

Browning, R., Li, T.Z., Chui, B., Jun Ye, Pease, R.F.W., Czyzewski, Z. & Joy, D.C. (1995). Low-energy electron/

https://doi.org/10.1017/S0263034604222091 Published online by Cambridge University Press

atom elastic scattering cross sections from 0.1–30 keV. *Scanning* **17**, 250–253.

Brunel, F. (1987). Not-so-resonant, resonant absorption. *Phys. Rev. Lett.* **59**, 52–55.

Casnati, E., Tartari, A. & Baraldi, C. (1982). An empirical approach to K-shell ionisation cross section by electrons. *J. Phys. B* **15**, 155–167.

Davies, J.R., Bell, A.R., Haines, M.G. & Guerin, S.M. (1997). Short-pulse high-intensity laser-generated fast electron transport into thick solid targets. *Phys. Rev. E* **56**, 7193–7203.

Davis, J., Clark, R. & Guiliani, J. (1995). Ultrashort-pulse laser-produced Al/Si plasma. *Laser Part. Beams* **13**, 3–18.

Dick, C.E., Lucas, A.C., Motz, J.M., Placious, R.C. & Sparrow, J. H. (1973). Large-angle L x-ray production by electrons. *J. App. Phys.* **44**, 815–826.

Eder, D.C., Pretzler, G., Fill, E., Eidmann, K. & Saemann, A. (2000). Spatial characteristics of K_α radiation from weakly relativistic laser plasmas. *Appl. Phys. B* **70**, 211–217.

Feurer, T., Morak, A., Uschmann, I., Ziener, C., Schwoerer, H., Förster, E. & Sauerbrey, R. (2001*a*). An incoherent sub-picosecond X-ray source for time-resolved X-ray-diffraction experiments. *Appl. Phys. B* **72**, 15–20.

Feurer, T., Morak, A., Uschmann, I., Ziener, C., Schwoerer, H., Reich, Ch., Gibbon, P., Förster, E., Sauerbrey, R., Ortner, K. & Becker, C.R. (2001*b*). Femtosecond silicon K_α pulses from laser-produced plasmas. *Phys. Rev. E* **65**, 016412.

Gibbon, P. & Förster, E. (1996). Short-pulse laser–plasma interactions. *Plasma Phys. Contr. Fusion* **38**, 769–793.

Hubbel, J.H. & Seltzer, S.M. (2001). Tables of X-ray mass attenuation coefficients and mass energy-absorption coefficients from 1 keV to 20 MeV for lements $Z = 1$ to 92 and 48 additional substances of dosimetric interest. National Institute for Standards and Technology, http://physics.nist.gov/PhysRefData/XrayMassCoef/cover.html.

Lichters, R., Pfund, R.E.W. & Meyer-ter-Vehn, J. (1997). LPIC++: A parallel one-dimensional relativistic electromagnetic particle-in-cell-code for simulating laser–plasma interactions, Report MPQ 225, Garching, Germany: Max-Planck Institut für Quantenoptik.

Limpouch, J., Bìna, V., Dytrych, T. & Klimo, O. (2002). Laser absorption, electron acceleration and *K*-α emission in short-pulse laser-target interactions. *Cz. J. Phys.* **52**, D342–D348.

Limpouch, J., Drska, L. & Liska, R. (1994). Fokker–Planck simulations of interactions of femtosecond laser pulses with dense plasmas. *Laser Part. Beams* **12**, 101–110.

Nakano, H., Nishikawa, T. & Uesugi, N. (2001). Enhanced *K*-shell x-ray line emissions from aluminium plasma created by a pair of femtosecond laser pulses. *Appl. Phys. Lett.* **79**, 24–26.

Namito, Y. & Hirayama, H. (1999). Implementation of electron-impact ionization into the EGS4 code. *Nucl. Instrum. Methods Phys. Res. A* **423**, 238–246.

Reich, Ch., Gibbon, P., Uschmann, I. & Förster, E. (2000). Yield optimization and time structure of femtosecond plasma K_α sources, *Phys. Rev. Lett.* **84**, 4846–4849.

Rose-Petruck, C., Jimenez, R., Guo, T., Cavalleri, A., Siders, C.W., Raksi, F., Squier, J.A., Walker, B.C., Wilson, K.R. & Barty, C.P.J. (1999). Picosecond–miliångström lattice dynamics measured by ultrafast X-ray diffraction. *Nature* **398**, 310–312.

Salvat, F., Fernandez-Varea, J.M., Acosta, E. & Sempau, J. (2001). PENELOPE—A code system for Monte Carlo simulation of electron and photon transport. In *Workshop Proceedings*, Nuclear Energy Agency.

Schlegel, Th., Bastiani, S., Gremillet, L., Audebert, P., Geindre, J.P., Gauthier, J.-C., Lefebre, E., Bonnaud, G. & Delettrez, J. (1999). Comparison of measured and calculated x-ray and hot-electron production in short-pulse laser–solid interactions at moderate intensities. *Phys. Rev. E* **60**, 2209–2217.

Siders, C.W., Cavalleri, A., Sokolowski-Tinten, K., Toth, C., Guo, T., Kammler, M., Horn von Hoegen, M., Wilson, K.R., Von der Linde, D. & Barty, C.P.J. (1999). Detection of nonthermal melting by ultrafast X-ray diffraction. *Science* **268**, 1340–1342.

Uschmann, I., Gibbon, P., Klöpfel, D., Feurer, T., Förster, E., Audebert, P., Geindre, J.P., Gauthier, J.-C., Rousse, A. & Rischel, C. (1999). X-ray emission produced by hot electrons from fs-laser produced plasma—Diagnostic and application. *Laser Part. Beams* **17**, 671–680.

Von der Linde, D., Sokolowski-Tinten, K., Blome, Ch., Dietrich, C., Zhou, P., Tarasevitch, A., Cavalleri, A., Siders, C.W., Barty, C.P.J., Squier, J., Wilson, K.R., Uschmann, I. & Förster, E. (2001). Generation and application of ultrashort X-ray pulses. *Laser Part. Beams* **19**, 15–22.

Zhidkov, A., Sasaki, A., Utsumi, T., Fukumoto, I., Tajima, T., Saito, F., Hironaka, Y., Nakamura, K.G., Kondo, K. & Yoshida, M. (2000). Prepulse effects on the interaction of intense femtosecond laser pulses with high-Z solids. *Phys. Rev. E* **62**, 7232–7240.

https://doi.org/10.1017/S0263034604222091 Published online by Cambridge University Press